Medical Robotics

Design, Modelling and Teleoperation of a 2 mm Diameter Compliant Instrument for the da Vinci Platform

P. FRANCIS, K. W. EASTWOOD, V. BODANI, T. LOOI, and J. M. DRAKE

Centre for Image-Guided Innovation & Therapeutic Intervention, The Hospital for Sick Children, Toronto, Canada

Associate Editor Daniel Elson oversaw the review of this article.

Abstract—This work explores the feasibility of creating and accurately controlling an instrument for robotic surgery with a 2 mm diameter and a three degree-of-freedom (DoF) wrist which is compatible with the da Vinci platform. The instrument's wrist is composed of a two DoF bending notched-nitinol tube pattern, for which a kinematic model has been developed. A base mechanism for controlling the wrist is designed for integration with the da Vinci Research Kit. A basic teleoperation task is successfully performed using two of the miniature instruments. The performance and accuracy of the instrument suggest that creating and accurately controlling a 2 mm diameter instrument is feasible and the design and modelling proposed in this work provide a basis for future miniature instrument development.

Keywords—Surgical robotics, Dexterous manipulators, Compliant joints, Miniature instruments.

INTRODUCTION

The introduction of robotics into surgery has led to many new technologies that enhance surgeons' dexterity and precision. For example, the da Vinci Surgical System has been shown to increase surgeon's dexterity up to 50% compared to manual laparoscopy.[13] In 2017, approximately 850,000 gynecological, urological and gastrointestinal da Vinci surgeries were performed world-wide.[7] However, the 5 and 8 mm shaft diameters of the existing instruments limit the system's use in pediatrics, neurosurgery, and otolaryngology.[9,11,12] These surgeries occur in very small operating volumes compared to the size of da Vinci tools, yet could significantly benefit from this technology. This work

presents the design and evaluation of a 3 degree of freedom (DoF) 2 mm diameter instrument compatible with the da Vinci platform.

There are a limited number of previously reported 3-DoF wristed surgical instruments with shaft diameters < 3 mm.[6,16] These designs are based on either linkage or compliant joint mechanisms, however, none employ notched nitinol tubes nor have they been integrated with the da Vinci platform. Notched nitinol tube joints are mechanisms composed of cuts used to achieve directional compliance and are often used for actuation at a reduced size due to their monolithic structure. Commonly, the notches are rectangular and are actuated using cables attached distal to the cuts. Most of the < 2 mm diameter designs involve cutting from one side of the tube past the midline, also referred to as asymmetric notches, to create a single-DoF joint.[2,5,15,17] Designs that are capable of multi-DoF bending are typically larger (> 4 mm) and involve symmetric notches positioned orthogonally.[14]

The instrument presented here describes a multi-DoF bending joint using a tube diameter < 2 mm which is controlled *via* a da Vinci Research Kit (dVRK).[8] Early concepts for the design and modelling of the instrument were introduced in prior work.[3,4] The contributions of this manuscript include; a detailed design motivation for the wrist, a formalized kinematics model, a detailed parameter selection of the wrist, experimental characterization and verification of the wrist, as well as a teleoperation task. The organization of the paper is as follows: The design and kinematic model of the wrist joint is defined followed by the selection of parameters which determine the joint's geometry. Next, the instrument's base mechanism which controls the wrist is detailed. An experimental assessment of the wrist's bending behaviour,

Address correspondence to P. Francis, Centre for Image-Guided Innovation & Therapeutic Intervention, The Hospital for Sick Children, Toronto, Canada. Electronic mail: p.francis@mail.utoronto.ca

force-transmission capabilities and model accuracy are included followed by a teleoperation task which involves operating the instrument within a bell pepper.

MATERIALS AND METHODS

Wrist Design

The wrist design presented here is a multi-DoF bending notched nitinol tube joint with square asymmetric notches arranged in a 120° spiral pattern, seen in Fig. 1. Square notches can be manufactured using low-cost micromachining, and the asymmetric design has the benefit of lower actuation forces and compact bending.[17] This notch pattern allows for a roll–pitch–yaw style wrist similar to existing da Vinci instruments. This joint design differs from other square asymmetric notched-tube joints by arranging the notches in multiple planes on the tube to achieve multi-DoF (pitch and yaw) bending while also to minimize coupling. An actuation cable is aligned with each of the three notch cutting planes. The cables are routed outside of the tube with small rings made from 0.15 mm steel wire wrapped around both the tube and the cables to maintain their position. This cable guide approach offers the advantage of simple assembly while minimally increasing the joint's overall diameter.

The 120° notch cutting pattern and cable locations were designed to minimize coupling between the three actuation cables such that each cable can only influence the aligned notches. Figure 2 provides a cross section of the joint and demonstrates the motivation for this design as it increases the desirable moment arm

while decreasing the undesirable moment arm in comparison to positioning the joints at 90° or routing the cables within the tube. The distance between the cable and the neutral bending plane of its corresponding actuated notch is approximately seven times that of the undesirable distance from the other cables to the same neutral bending plane.

With the 120° cutting pattern, there are three primary bending directions toward each of the three cables. Bending in between these primary directions is achieved by actuating two of the cables simultaneously. In this case, the notches aligned with the two actuated cables will bend while the remaining set of notches aligned with the unactuated cable remain unbent. This assumption is explored in the "Offset Distance and Coupling" section. This scheme results in at most two of the three cables being actuated at any given time to achieve 2-DoF bending, that is to bend in any direction. Controlling this unique wrist design requires a new kinematic model which can predict the joint's complex bending behavior and multi-cable actuation.

Wrist Kinematics

The kinematics proposed for this joint design models each notch as having a constant curvature and the overall shape of the joint is expressed as a series of transformations. The model for the deformed shape of an individual notch has been derived by York *et al.* and validated based on a 1-DoF joint composed of a series of square asymmetric notches.[18] Here, we extend this model to a multi-DoF, multi-cable joint design, as shown in Fig. 3.

From Ref. 18, the curvature and arc length across a single notch can be derived from the cable displacement. The first modification to the kinematics accounts for the change in cable position to the outside of the
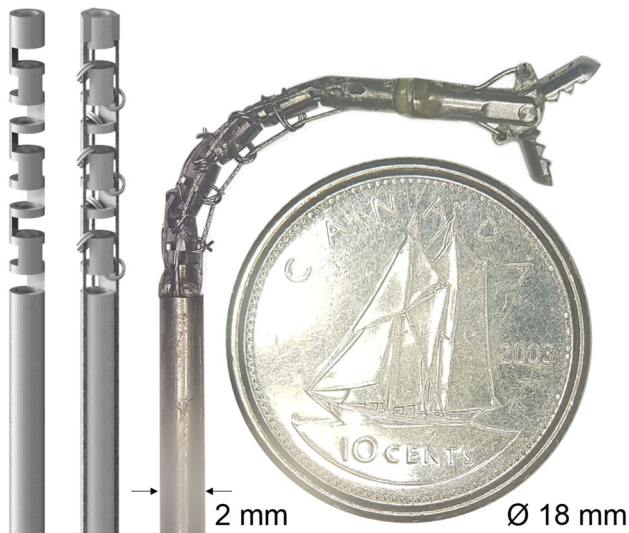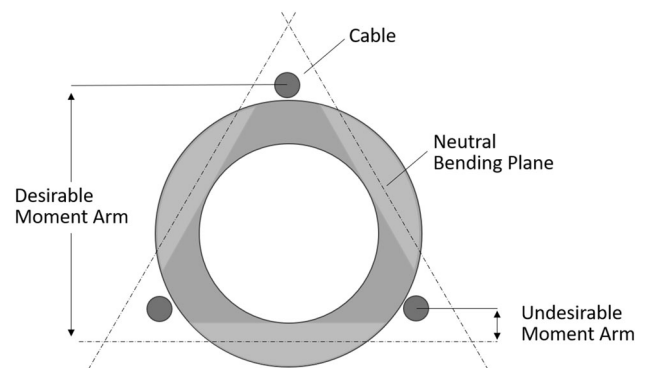

FIGURE 1. Notched-nitinol tube joint design for instrument's wrist with 120° notch spacing, three cables and cable guides at a 2 mm overall diameter.

FIGURE 2. Joint cross-section illustrating the large desirable moment arm compared to the small undesirable moment arm.

tube, resulting in a new equation for an individual notch's curvature:

$$\kappa \approx \frac{\Delta l}{h(d + \epsilon_{cm} + \bar{y}) - \Delta l \bar{y}}. \tag{1}$$

Note that this equation uses a small-angle approximation. The term ϵ_{cm} is used to account for the cable migrating away from the outer wall when the notch is actuated. This behaviour can be seen in Fig. 1. The value of ϵ_{cm} can be determined as the inner diameter of the cable guide rings minus the tube wall thickness. The transformation matrix across a single notch, based on κ and s, remains the same as in Ref. 18:

$$T_j^{j+1} = \begin{bmatrix} 1 & 0 & 0 & 0 \\ 0 & \cos(\kappa s) & -\sin(\kappa s) & \frac{\cos(\kappa s) - 1}{\kappa} \\ 0 & \sin(\kappa s) & \cos(\kappa s) & \frac{\sin(\kappa s)}{\kappa} \\ 0 & 0 & 0 & 1 \end{bmatrix}. \tag{2}$$

This transformation is used for the proposed modified kinematics when considering each individual notch's bending behaviour. From Ref. 18, the contribution of multiple notches in a single-DoF joint is represented as:

$$T_{\text{wrist1}-\text{DoF}} = \prod_{j=1}^{\# \text{ of notches}} T_j^{j+1} T_c \tag{3}$$

where T_c in the single-DoF bending case, is a transformation defining a linear translation along the z-axis by the notch spacing, c. The second modification

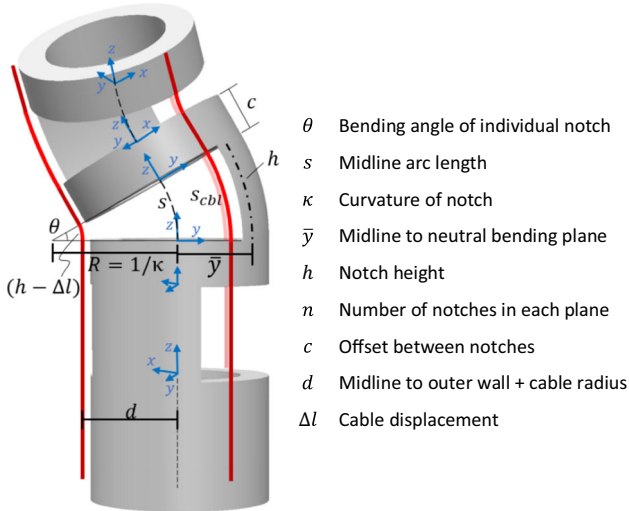|		
θ	Bending angle of individual notch
s	Midline arc length
κ	Curvature of notch
$\bar{y}$	Midline to neutral bending plane
h	Notch height
n	Number of notches in each plane
c	Offset between notches
d	Midline to outer wall + cable radius
Δl	Cable displacement

FIGURE 3. Multi-DoF square notch joint segment. The parameters defining the notch are the same as those used in Ref. 18.

required for this multi-DoF joint is to account for a rotation of $120°$ about the z-axis:

$$T_c = \begin{bmatrix} \cos(120°) & -\sin(120°) & 0 & 0 \\ \sin(120°) & \cos(120°) & 0 & 0 \\ 0 & 0 & 1 & c \\ 0 & 0 & 0 & 1 \end{bmatrix}. \tag{4}$$

Third, the multi-DoF bending wrist joint is composed of a series of three notch segments, like the one in Fig. 3, where the three notches bend independently of each other, and based on their aligned cable's displacement. T_{seg} is the transformation matrix across a single three notch segment;

$$T_{\text{seg}} = T_1 T_c T_2 T_c T_3 T_c \quad \text{where } T_{1,2 \text{ and } 3} = T_i(\Delta l_i) \tag{5}$$

Here, each transformation across the notch ($T_{1,2 \text{ and } 3}$) is a function of the cable that notch aligns with. To calculate the joint's overall transformation, accounting for all of the notches on the wrist, the transformation becomes:

$$T_{\text{wrist multi}-\text{DOF}} = \left(T_{\text{seg}}\right)^n, \tag{6}$$

where n is the number of cuts in each direction, and the total number of cuts is $3n$. Similar to Ref. 18, this model assumes that each notch closes equally.

The fourth modification accounts for changes in the length of the tube's midline depending on the bending configuration. Due to the nature of asymmetric notches, the tube's midline across the notch will shorten the more the notch is bent. Considering the case where one of the three cables is actuated, the path of the other two cables will shorten across the actuated notches. This can be seen in Fig. 3 where the red cables to the right have a shorter path across the middle notch compared to an unactuated notch. To account for this, the displacement of each of the three cables will be the sum of the kinematic length ($n\Delta l_i$) and a slack variable (l_{si}). The slack compensation is necessary for the actuated cables when more than one cable is being actuated. To solve, the length of the cable across a notch which that cable is not actuating, $s_{\text{cbl}\sim i}$, is determined using the arc length formula:

$$s_i \kappa_i = \frac{s_{\text{cbl}\sim i}}{\frac{1}{\kappa_i} + d \sin 30°}, \tag{7}$$

$$s_{\text{cbl}\sim i} = s_i \left(1 + \frac{\kappa_i d}{2}\right), \tag{8}$$

where the subscript $\sim i$ denotes the indices that are not i. Using Fig. 3 as an example, the parameters defining the notch being actuated (e.g., $i = 2$) would be s_2 and κ_2 and the path length of cables 1 and 3 across the notch are being solved.

To calculate l_{si}, accounting for all instances where slack is introduced, it is the shape of the other notches that must be considered for a given cable. The cables and their aligned notch parameters are assigned a subscript 1–3. The shortening of a cable across the wrist can be calculated as follows:

$$l_{\mathrm{si}} = n(2h - s_{\mathrm{cbl}\sim a} - s_{\mathrm{cbl}\sim b}), \qquad (9)$$

where the subscripts a and b represent the two indices that are not i. For example, l_{s1} is a function of $s_{\mathrm{cbl}\sim2}$ and $s_{\mathrm{cbl}\sim3}$.

Lastly, the total cable displacement can be calculated as the sum of the displacement from the kinematics and the additional cable displacement.

$$\Delta l_{\mathrm{totali}} = n\Delta l_i + l_{\mathrm{si}}. \qquad (10)$$

Without this adjustment, the cables could be shortened with the expectation that it would deflect the joint but only slack would be removed.

Parameter Selection and Finite Element Analysis

With a design and kinematic model for the 3-DoF wrist, the joint's parameters are selected to meet the instrument's criteria listed in Table 1. Joint coupling must also be evaluated. The finite element analysis (FEA) package ANSYS 18.0 Research Version (ANSYS, Inc., Canonsburg, PA, USA) is used to aid the parameter selection and coupling evaluation using the simulation setup outlined in the following section.

Finite Element Analysis Setup

The joint models were developed and imported from SolidWorks (Dassault Systèmes, Waltham, MA, USA) and meshed with elements of type Solid186. Between simulations, the mesh size varied in the range of 0.05 to 0.15 mm to ensure convergence of a solution. To simulate notch actuation, an actuation cable was modelled and fixed to the tip of the joint and displaced to reproduce the true behavior of the physical joints. The notch and cable models were connected using a spot weld contact, and a frictional contact was specified with a coefficient of friction of 0.3 between the outer surface of the cable and the tube. When the simulations were symmetric, only half of the modelled joint was simulated, as shown in Fig. 4. In these cases, symmetry constraint conditions were applied along the tubes' plane of symmetry, and a rigid constraint was implemented to fix the joint's base.

The notch joint's material constitutive model was implemented as a custom shape memory alloy of super-elasticity type, and the parameters are outlined in Table 2. The constitutive model for the steel actuation cable is summarized in Table 3.
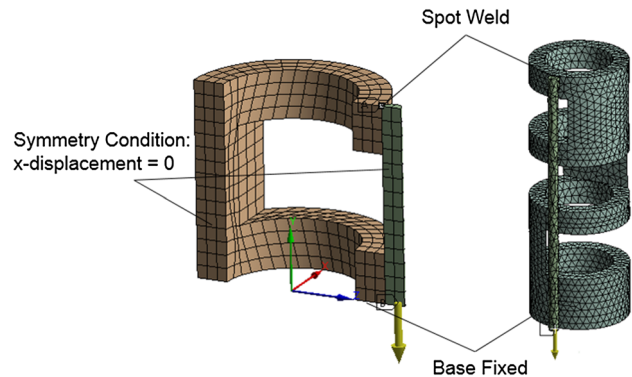

FIGURE 4. ANSYS joint loading. The model on the left is used for defining the cut depth. The model on the right is used to define the offset distance and detect coupling.

TABLE 1. Wrist design requirements.

Constraints	Values
Instrument outer diameter	2 mm
Achievable bending angle in every direction	80°
Maximum strain (conservative estimate)	6%

TABLE 2. Constitutive model of selected nitinol tube provided by the supplier.

ANSYS model parameters	Values
Young's modulus of the austenite phase (E)	61.8 GPa
Poisson's ratio (v)	0.3
Material response ratio between tension and compression (α)	0
Maximum residual strain (ε_l)	0.05
Starting stress value for the forward phase transformation (σ_{SAS})	578 MPa
Final stress value for the forward phase transformation (σ_{FAS})	580 MPa
Starting stress value for the reverse phase transformation (σ_{SSA})	273 MPa
Final stress value for the reverse phase transformation (σ_{FSA})	242 MPa

TABLE 3. Constitutive model of steel from ANSYS.

ANSYS model parameters	Values
Young's modulus (E)	200 GPa
Poisson's ratio (v)	0.3
Yield stress (σ_{yield})	250 MPa

Tube Diameter, Notch Depth, Notch Height and Number of Notches

The tube size is selected to achieve an overall diameter of 2 mm. Since the cable and guide wire are 0.15 mm in diameter, a 1.4 mm tube outer diameter is desired. Based on the tube sizes readily available, a 1.37 mm outer diameter tube is selected with an inner diameter of 0.94 mm. The depth of cut for the notches is selected based on the maximum strain seen at closure of the notch. The manufacturer of the procured nitinol tube suggests the elastic strain limit is some value above 6%. FEA is used to determine a notch depth that results in 6% strain at full closure. A single notch is modelled and the notch depth is varied from 80 to 90% of the outer diameter at 2.5% intervals with the maximum equivalent strain recorded when the notch is fully closed, seen in Fig. 5. The offset length and notch height were arbitrarily selected as 25 and 50% of the tube's outer diameter, respectively, since maximum strain is primarily independent of notch height.[18]

The notch depth at 85% (1.16 mm) is associated with a strain value just below 6%. This is the value that is selected which has a resulting neutral bending axis location, $\bar{y}$, of 0.56 mm.

The notch height, h, and number of notches in each plane, n, are selected based primarily on the maximum bending angle of the joint. From the kinematics, the maximum bending angle in between the primary bending directions is approximately 15% less than along the primary bending directions. As a result, a maximum bending angle of 90° along the primary bending directions is selected with the smallest maximum bending angle considering all directions being 77°. This is considered adequately close to 80°. In an effort to achieve the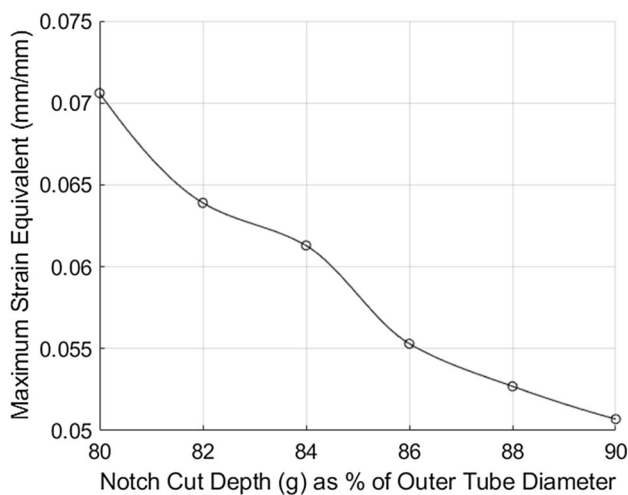 most compact joint possible while still maintaining good predictability in the joint's bending behaviour, a maximum bending angle of 30° for a single notch is selected. This has an associated notch height of 0.66 mm, assuming constant curvature bending. The number of notches in each bending plane is therefore three for a total of nine notches to make up the wrist joint.

Offset Distance and Coupling

Selecting an offset distance between the notches that is too small results in an unintended region of bending, affecting the coupling of the wrist. However, large offset distances reduce the compactness of the joint. An FEA study is conducted to determine the affect of the offset distance on joint coupling using a three notch tube segment. The offset distance, c, is varied from 100% (0.22 mm) to 200% (0.43 mm) of the intended bending section's width (OD-g) at 20% increments. The modelled joint segment is actuated by a cable aligned with the middle notch such that it fully closes. The angle of each notch is measured to determine the presence of coupling. Images and a plot of the results are included in Fig. 6.

The smallest offset length which provided less than 3° of coupling is 1.65 times (OD-g) or 0.34 mm. This value provides a compromise between good decoupling of the joint while still achieving a compact joint.

FEA Model Accuracy Comparison

To assess the accuracy of the FEA studies, the simulation results were directly compared with the behaviour of a physical specimen. A single notch cut using the selected parameters was loaded with a cable running on the inside of the tube. A model of the notch was simulated in ANSYS with the same loading condition. Note that this is the only simulation with the cable positioned within the tube. Figure 7 compares the cable displacement vs. bending angle as well as the cable actuation tension vs. bending angle for the final notch geometry selected for fabrication.

The similarity between the FEA and experimental results provide confidence that the FEA studies are sufficient to predict the behaviour of the resulting multi-notch tool.

Parameter Selection Summary and Manufacturing

Table 4 summarizes the defined parameters used to fabricate the joint prototype. The tube was cut on a benchtop CNC (Minitech Machinery, USA) from a nickel–titanium alloy (Nitinol) tube (NDC, Confluent Medical Technologies, USA). The wrist is actuated using braided stainless-steel cables (Sava, Inc., USA) which are soldered in place.

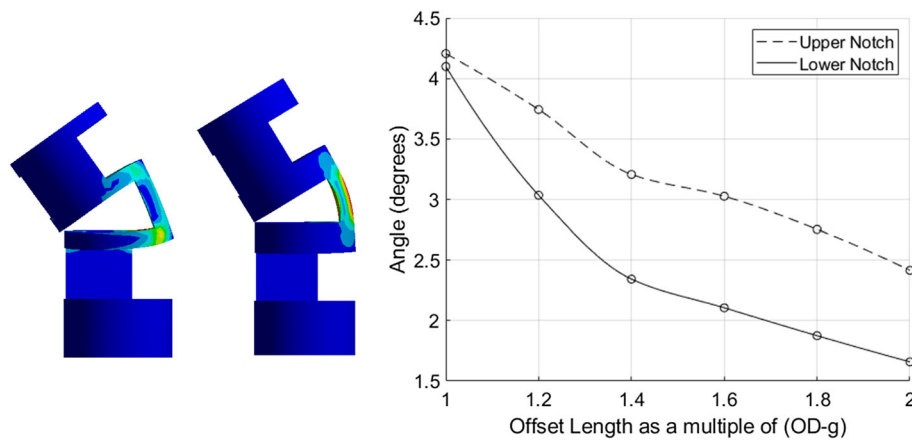FIGURE 5. Notch depth vs. maximum strain at notch closure.

FIGURE 6. Joint coupling based on offset length. At left, bending behaviour for two joint sections with varying offset lengths, with colour representing strain. The joint to the left has an offset length of (*OD-g*) while the joint to the right has an offset length of 2(*OD-g*). The plot shows offset length vs. angle of the unactuated notches when the middle notch is actuated to fully close.
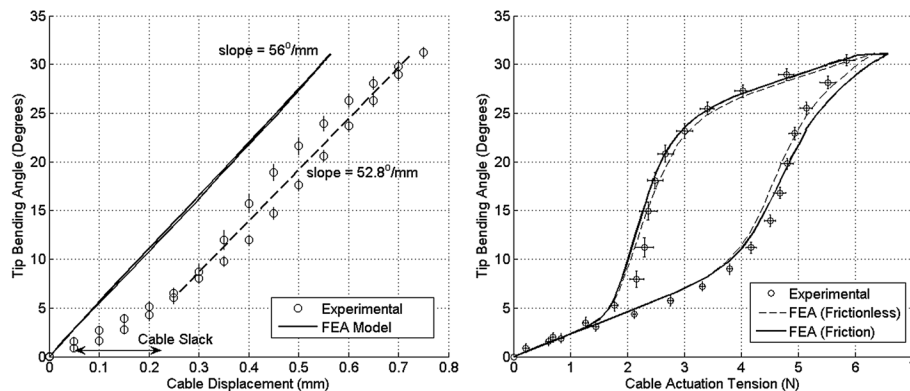

FIGURE 7. Left: FEA and experimental cable displacement and right: FEA and experimental cable tension comparison.

TABLE 4. Parameter selection summary.

Parameters	Values
Tube outer diameter	1.37 mm
Tube inner diameter	0.94 mm
Notch depth, g	1.16 mm
Midline to neutral bending plane, $\bar{y}$	0.56 mm
Notch height, h	0.66 mm
Number of notches in each plane, n	3
Offset, c	0.34 mm
Midline to cable distance, d	0.76 mm
Total joint length	8.66 mm
Actuation cable diameter	0.15 mm
Cable guide wire diameter	0.15 mm

Instrument Base Design

All instruments compatible with the dVRK have a common adaptor that allows the tools to be rapidly interchanged on the patient-side-manipulator (PSM) of the da Vinci robot. This adaptor uses four revolute actuation disks, limited to ± 170°, to transmit input torques from the PSM to the tool's DoF.[3] An instrument base was designed using this standardized interface to convert the inputs from the actuation disks into the instrument's roll, pitch–yaw and end-effector DoF. Two actuation disks are used to control roll and actuation of the end-effector, and two actuation disks are used for pitch–yaw bending. Since the design of the wrist uses three cables to actuate bending, there is a design challenge to develop a mechanism capable of actuating three cables with two actuation disks.

To control the wrist, at most two cables are needed to actuate bending while the third cable can maintain its length. Also, the wrist configuration that requires the longest length of cable is the straight configuration. Using this information, Fig. 8 shows the "wiper" mechanism that has been proposed to control the wrist. Two "wipers" can pivot, like the wind-shield wipers of a car, to push on the adjacent cable routes and increase their path length at the base. With these
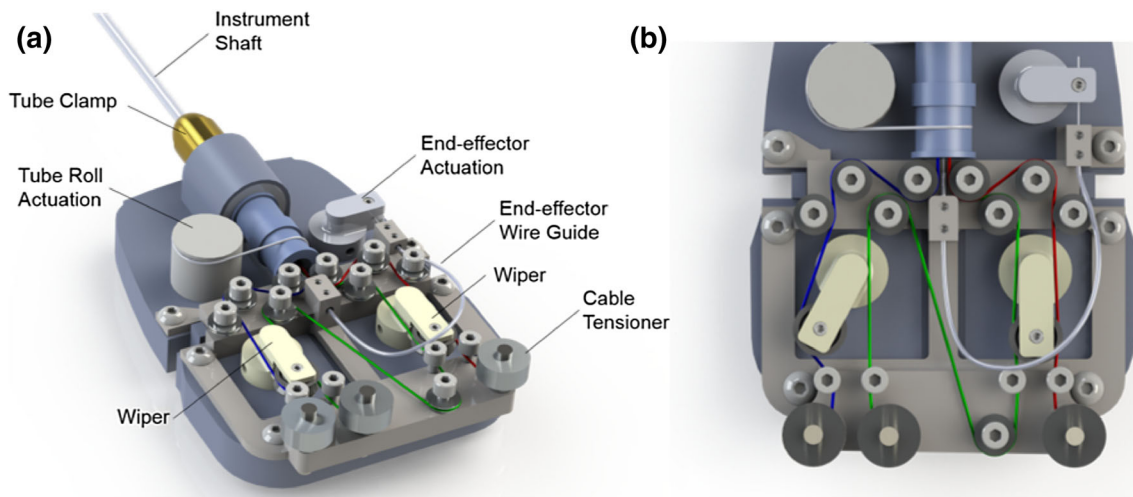
FIGURE 8. Instrument base design with wiper mechanism: (a) components of instrument base and (b) wiper mechanism with left wiper actuating the blue cable. The four actuation disks would be located on the bottom side of the instrument's base beneath each of the four actuation components.
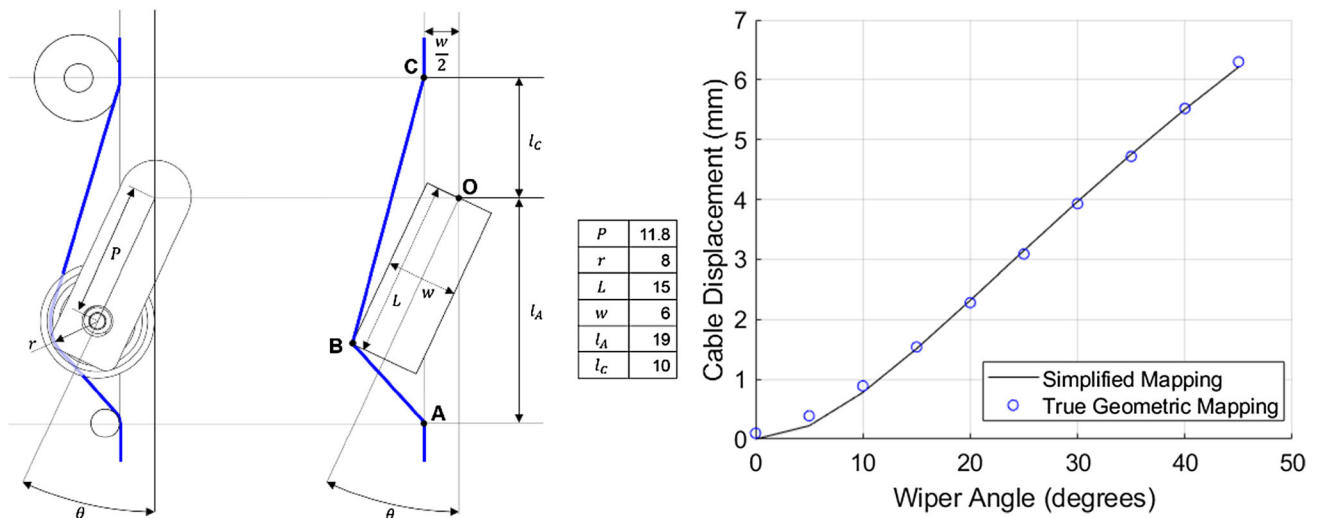

FIGURE 9. Wiper kinematic mapping. Left wiper diagram illustrates the true wiper geometry and cable path in blue alongside the simplified geometry used for the kinematics. Dimensions are in millimetres. The plot illustrates wiper angle vs. cable displacement for the two cases, up to 6 mm cable displacement. The selected wrist configuration is expected to remain below 4 mm cable displacement.

two wipers, any two of the three cables can be actuated at any given time, and by any amount. This is particularly valuable given the complexity of the cable displacement kinematics due to the wrist's changing midline length.

Wiper Mechanism Kinematics

The angle of each wiper (θ) corresponds with a resulting cable displacement (Δl). To generate an analytical relationship, the cable is assumed to follow a straight line between three points, A, B, and C as shown in Fig. 9.

To solve for the change in cable length, the location of point B is solved based on the angle of the wiper, θ:

$$B = \left(L\sin\theta + \frac{w}{2}\cos\theta,\, L\cos\theta - \frac{w}{2}\sin\theta \right).$$

The cable displacement is therefore:

$$\Delta l = (AB + BC) - AC$$

where AC represents the unactuated cable length. A plot of the wiper angle vs. cable displacement is shown in Fig. 9. The blue line represents the algebraic solution described here, and the red points represent the true geometric results, which includes the curved paths
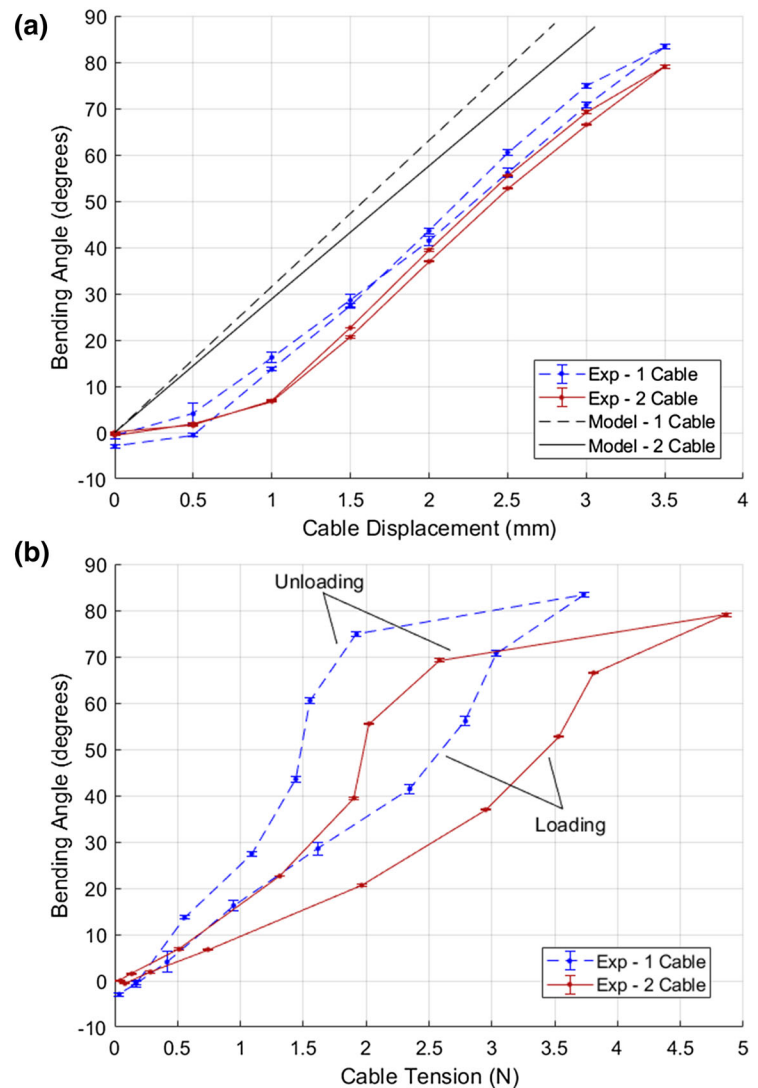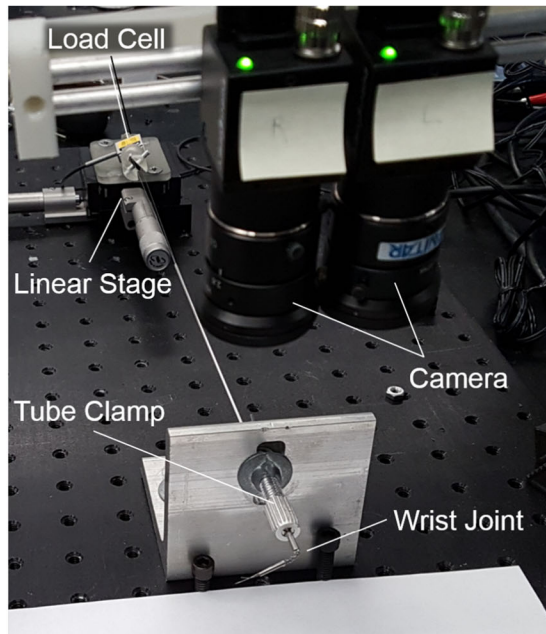
FIGURE 10. Cable displacement and tension vs. bending angle and radius. (a) Cable displacement vs. bending angle for single and double cable actuation. The offset can be attributed to cable stretch. (b) Cable tension vs. bending angle for single and double cable actuation.

for the post at point A, the pulley on the wiper at point B, as well as the pulley at point C. The data was generated using a SolidWorks Sketch. The average error between the results from 0° to 45° is 0.067 mm. This error is acceptable and validates the use of the simplified algebraic approach.

RESULTS

Characterization of Wrist Performance

The performance of the wrist has been assessed in three parts. First, the range of motion and bending behaviour of the 2-DoF asymmetric notch joint is characterized. Next, the joint's force transmission

capabilities are quantified, and finally, the accuracy of the wrist's kinematics model is measured.

Cable Displacement and Tension vs. Bending Angle and Radius

The experimental setup shown in Fig. 10 was used to measure the relationship between the joint inputs, cable displacement and cable tension, and the joint outputs, bending angle and bending radius.

To measure the shape of the wrist, two Flea3 1.3 MP cameras (Point Grey, Vancouver, Canada) were arranged in a stereo-configuration and calibrated using the MATLAB® Camera Calibration Toolbox. A 460P Series linear stage (Newport Corporation, Irvine, California, US) with an FSH00095 JR S-Beam Load

Cell (FUTEK, USA) was used to control the wrist's actuation cables.

The linear stage was translated in 0.5 mm increments, and the cable tension and wrist shape was recorded. The wrist was actuated from straight to approximately 80°, with measurements repeated five times and averaged. Two cases were evaluated: first, a single cable was actuated and the wrist's bending along one of the primary bending planes was assessed. Second, two cables were actuated simultaneously to assess bending directly in between primary bending planes. For the double cable actuation, tension was applied equally to both cables, and the output recorded by the sensor represents the sum of the tension applied to both cables. The results are presented in Figs. 10a and 10b. The minimum bending radius was measured to be 5.27 and 4.95 mm, for single and double cable actuation, respectively.

Cable Tension vs. Force Output at Tip

A similar experimental setup to Fig. 10 was used to characterize the relationship between the wrist's input cable tension and the force output at the instrument's tip. A modified multi-axis Gamma Force/Torque Sensor (ATI Industrial Automation, USA) was positioned at the wrist's tip to measure the force output of the wrist. The sensor was modified to include a plate with a small hole (1.59 mm diameter, 2 mm depth) that the instrument end-effector fit inside to measure the lateral forces (not plunging) applied by the wrist.

The instrument actuation cables were tensioned in increments of 0.5 N, measured using the FSH00095 load cell, and the tip forces were recorded. Tension was applied until the wrist began to retract rather than maintain an arc shape. The wrist was assessed in three different starting positions, with initial tip bending angles of 90°, 45° and 0°, for both single and double cable actuation. Table 5 summarizes the force range for each configuration.

Kinematic Model Accuracy for Wrist Joint

The accuracy of the kinematics model was assessed across the wrist's joint variables using Monte Carlo methods generating 135 points within a 65° bending angle. The wrist was commanded to each point where the predicted position and orientation was compared with the measured position and orientation.

To perform the experiment, the tool was mounted on the PSM and controlled using the dVRK's sawIntuitiveResearchKit v1.4.0 open-source software. The wrist was positioned above an Aurora (NDI Medical, Canada) electromagnetic tracker and a 6-DoF sensor was secured to the tip of the tool. The PSM was held fixed and only the wrist was actuated. Table 6 summarizes the position and orientation errors and Fig. 11 displays the evaluated workspace of the wrist.

TABLE 6. Error values between measured tip positions and orientations with the proposed kinematic model for the wrist joint.

	Position (mm)	Orientation
Mean	0.64	(7.2°, 5.7°, 8.1°)
95th Percent	1.36	(14.8°, 12.8°, 17.6°)

The 95th percentile error approaches the worst-case bound on wrist performance.

TABLE 5. Blocking force output data summary.

Angle (°)	Max force applied (associated actuation tension) (N)	
	Loading	Unloading
Single cable		
−90	0.26 (7)	0.36 (0)
−45	0.37 (6.5)	0.25 (0)
0	0.29 (5)	0 (0)
Double cable		
90	0.38 (8)	0.27 (0)
45	0.45 (7)	0.25 (0)
0	0.15 (6.5)	0 (0)
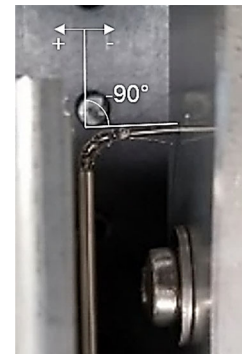
The associated image displays the joint actuated by a single cable, positioned at −90°.

Teleoperation

To evaluate the performance of the instrument in a surgical scenario, a clinical simulation was set up using a bell pepper, which have been used for endoscopic third ventriculostomy training. Figure 12 shows the experimental setup, which includes two 2 mm instruments, one with biopsy forceps and the other with scissors. These push–pull wire-actuated end-effectors were taken from existing manual tools and integrated with the instruments. Three ports were cut into the pepper, one for each instrument, and the third for an endoscope. The instruments were teleoperated using the dVRK's master manipulators.

The objective of the simulation was to dissect the seeds from the top of the pepper. This task required both instruments working in coordination; the forceps for grasping the seeds and the scissors to cut away the surrounding wall. The task also included a pick and place of the seeds allowing for qualitative assessment of instruments' dexterity and accuracy. The teleoperation task was performed for 23 min; a video segment is included with this paper.

Figure 13 includes images of the teleoperation task from the view of the endoscope. For comparison, an image of standard da Vinci instruments within the bell pepper cavity is included.

DISCUSSION

This work presents the development of a 2 mm diameter instrument with a 3-DoF wrist for the dVRK, including the wrist and base design, its kinematics as well as parameter selection to meet the design criteria. Four experiments were conducted to characterize the performance of the instrument's wrist. This work builds on previous work described in Refs. 3 and 4.

The wrist design incorporates a cable guide approach which offers a simple means to constrain the cables without significantly adding bulk to the overall diameter. Given that the primary benefit of notched-tube mechanisms is that they consist of a single monolithic structure, the cable guide rings are a simple add-on to achieve the desired result. Alternative approaches such as multiple disks similar to Refs. 16 and 6 which might fit around the tube would complicate the manufacturing and assembly significantly. Future iterations of the wrist should include more guide points along the joint.

The first experiment characterizes the bending behaviour of the wrist based on cable displacement and tension. These results provide a quantitative measure of the input–output relationship for the wrist joint. The cable-tension vs. joint angle plot demonstrates a nonlinear relationship with significant hysteresis in the loading vs. unloading directions. The cable displacement plot exhibits a linear input–output relationship with significantly less hysteresis. These findings support the approach used to control the wrist based on cable displacement kinematics. However, the presence of cable stretch offsets the lines from the model. Accounting for this offset can be done empirically, as was the case for the accuracy testing.

The second experiment characterized the force output range of the joint in various configurations. The results suggest that throughout the joint's range of motion, the joint can transmit at least 0.15 N laterally at the tip of the end-effector. Of the configurations measured, actuating the tip from a straight position in between two of the primary bending planes is the weakest direction, while the maximum force of 0.45 N
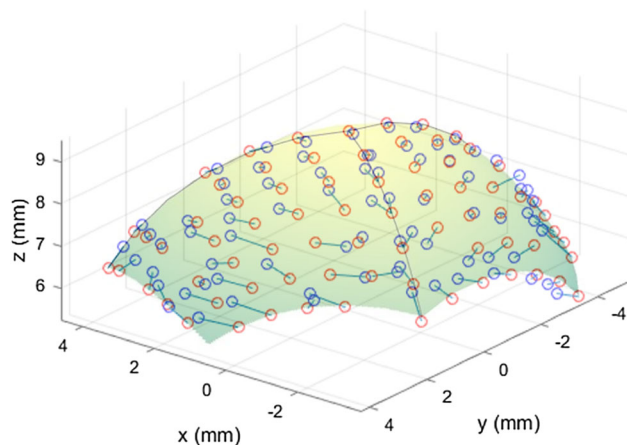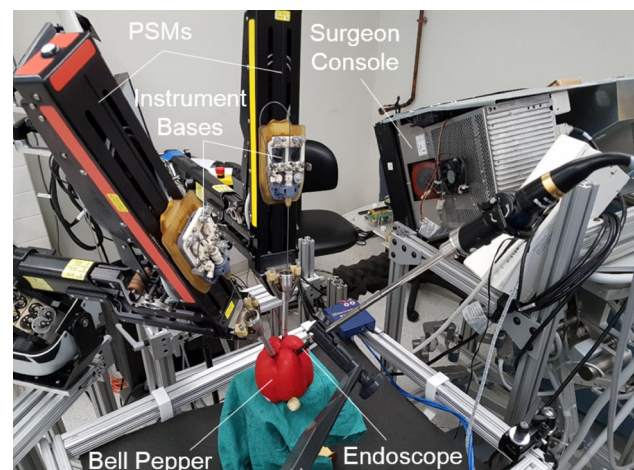

FIGURE 11. Evaluated workspace showing a subset of the predicted (red) and measured (blue) positions overlaid on the analytical workspace. The black lines denote the three primary bending directions.

FIGURE 12. Experimental setup for teleoperation task within bell pepper.
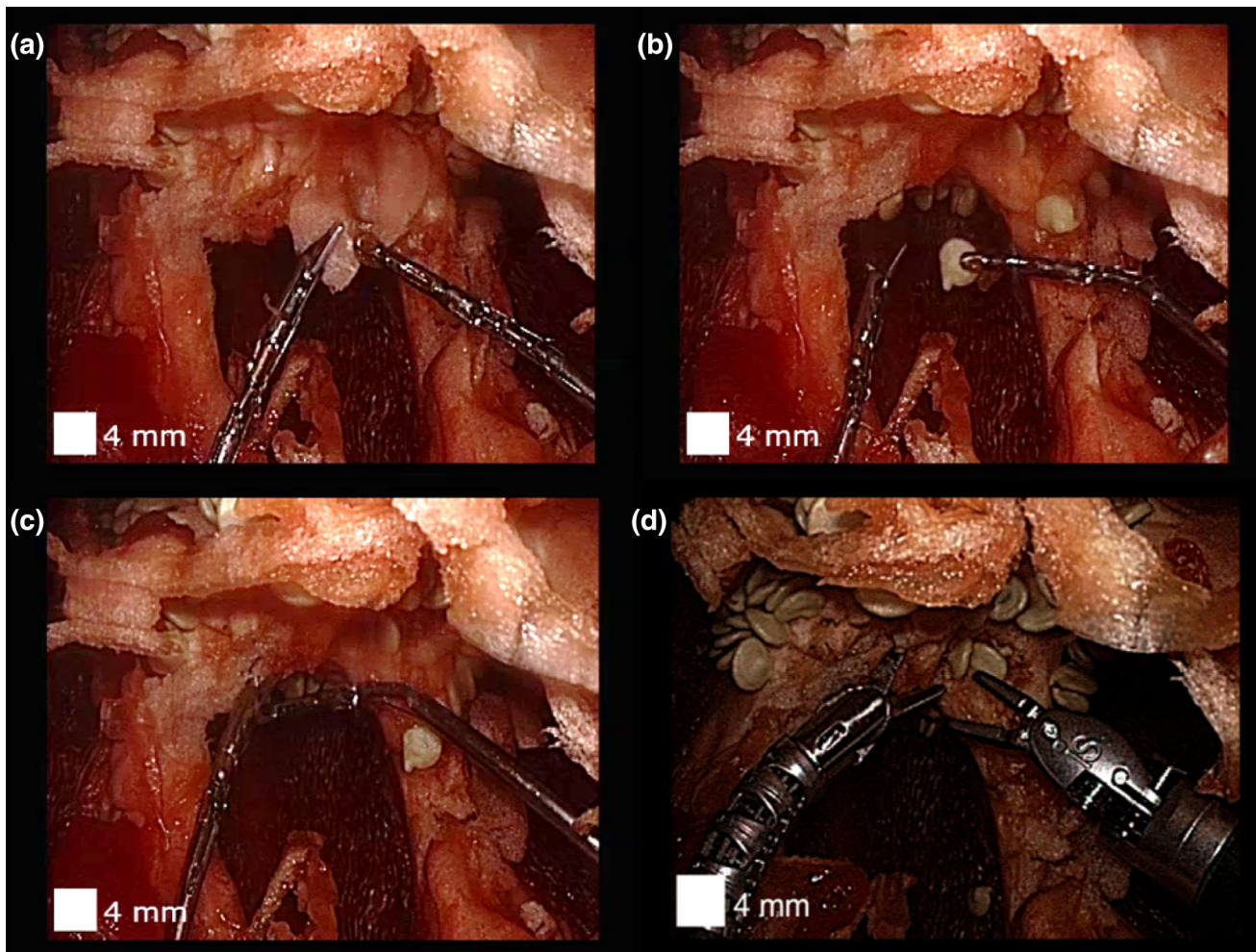
FIGURE 13. Endoscopic view of teleoperation task: (a) image shows right instrument biopsy forceps grasp a piece of flesh while left instrument scissors cut through the flesh, (b) image shows pick-and-place of the seeds, (c) image shows instruments working in very close proximity and (d) existing EndoWrist Instruments within bell pepper cavity for size comparison (5 mm on left and 8 mm on right).

was reached at a 45° angle when two cables are contributing equally and pushing in the direction of the bend. Using the requirements of neurosurgery as an example, the peak forces for manipulating brain tissue range from 0.01 to 0.5 N.[1,10] Currently, the instrument may be capable of performing a subset of neurosurgical procedures. The maximum cable tension from the first two experiments was 7 N which occurred when a single cable was generating a 0.26 N force. This maximum tension remains well below the cable's minimum breaking strength of 22.6 N.

The accuracy experiment, comparing the measured wrist tip position and orientation with the kinematic model, demonstrated errors within an acceptable range. For position and orientation error, 95% of the measurements were less than 1.36 mm and 15° and the mean error is 0.64 mm and 7°, respectively. This performance is adequate for initial development but

will require improvement in future design iterations. New measurement techniques may be necessary to evaluate the accuracy as the average position errors are approaching the resolution of the sensor at 0.48 mm RMS. Further, given that the instrument is a wrist intended to achieve a range of orientations within a small volume, improving the orientation error should be the focus.

The teleoperation task demonstrated that the instruments are successfully capable of operating in a confined volume, and have adequate space to work in coordination. The 2 mm OD allows the instruments to work in very close proximity, as was seen in the cases where the forceps manipulated the 4 mm diameter seeds while the scissors cut the seeds away from their base. The force output from instruments were sufficiently high enough to allow grasping and cutting of the pepper's flesh. Further, coupling between the end-

effector actuation and wrist bending was insignificant, and largely unnoticeable.

The main limitations of the physical validation experiments relate to the methods used to measure the wrist's position. The stereo-cameras were calibrated to allow for the selection of points on the images, and to convert this data into Cartesian coordinates using MATLAB®. However, the resolution of the cameras led to some uncertainty in selecting the same point locations on the tube between the two images. Further, the multi-axis force sensor also drifted over time. As these experiments are intended to provide a general range for the maximum output-force of the wrist, the effect of the drift was deemed sufficiently small. Moreover, every effort was made to perform the tests rapidly and zero the sensor whenever possible.

The major limitations of the kinematics accuracy experiment include manufacturing errors, sensing errors and the challenge of defining the actuator position associated with a cable displacement of zero. First, the machining methods used for joint fabrication introduce variability between the cut depths of each notch, as well as differences in the shape of the notch depending on end-mill wear. Further, differences in the size of the cable guide rings may also affect friction and the lateral movement of the cable. In terms of sensing, the rated error for the NDI Aurora's 6-DoF sensors is 0.48 mm RMS and 0.3° RMS. Given the size of the wrist's workspace, the rated position error is significant. Lastly, defining the zero-cable-displacement position, without any slack, is highly ambiguous. As slack is removed from the cable, friction in the line may result in applying a small force to the joint. To address this issue, the zero position was determined iteratively based on how well the calibration data, used to register the tool to the kinematics, matched the model. Specifically, the maximum bending angles were used for guidance.

Implementing the wrist as a da Vinci instrument has multiple advantages. First, the dVRK significantly accelerated the development toward teleoperation. Additionally, this approach may increase the likelihood of the research being implemented clinically by designing a device that is compatible with a widespread robotic system. Alternative implementations of this wrist could include incorporating it at the distal end of a concentric tube robotic system similar to[17] as well as integrating it with hand-held instruments. This research has attempted to further expand the potential of robotic surgery by discovering what is possible regarding dexterity and articulation at the 2 mm scale. Very few 3-DoF wrists with an active end-effector have been built and teleoperated at this scale which motivated the project. Future development of this instru-

ment has the potential to enable new surgical applications to benefit from robotic surgery.

ELECTRONIC SUPPLEMENTARY MATERIAL

The online version of this article (doi:https://doi.org/10.1007/s10439-018-2036-4) contains supplementary material, which is available to authorized users.

REFERENCES

[1]Bekeny, J. R., P. J. Swaney, R. J. Webster, III, P. T. Russell, and K. D. Weaver. Forces applied at the skull base during transnasal endoscopic transsphenoidal pituitary tumor excision. *J. Neurol. Surg. B* 74:337–341, 2013.
[2]Fichera, L., N. P. Dillon, D. Zhang, I. S. Godage, M. A. Siebold, B. I. Hartley, J. H. Noble, P. T. Russell, R. F. Labadie, and R. J. Webster. Through the eustachian tube and beyond: a new miniature robotic endoscope to see into the middle ear. *IEEE Robot. Autom. Lett.* 2(3):1488–1494, 2017.
[3]Francis, P., K. W. Eastwood, V. Bodani, K. Price, K. Upadhyaya, D. Podolsky, H. Azimian, T. Looi, and J. Drake. Miniaturized instruments for the da Vinci Research Kit: design and implementation of custom continuum tools. *IEEE Robot. Autom. Mag.* 24(2):24–33, 2017.
[4]Francis, P., K. W. Eastwood, V. Bodani, T. Looi, and J. M. Drake. Design and kinematic modelling of a miniature compliant wrist for the da Vinci Research Kit. In: The Hamlyn Symposium on Medical Robotics, 2017, pp. 41–42.
[5]Haga, Y., Y. Muyari, S. Goto, T. Matsunaga, and M. Esashi. Development of minimally invasive medical tools using laser processing on cylindrical substrates. *Electr. Eng. Jpn* 176(1):65–74, 2011.
[6]Harada, K., Z. Bo, S. Enosawa, T. Chiba, and M. G. Fujie. Bending laser manipulator for intrauterine surgery and viscoelastic model of fetal rat tissue. In: Proceedings 2007 IEEE International Conference on Robotics and Automation, 2007, pp. 611–616.
[7]Intuitive Surgical Annual Report 2017, 2017.
[8]Kazanzides, P., Z. Chen, A. Deguet, G. S. Fischer, R. H. Taylor, and S. P. DiMaio. An open-source research kit for the da Vinci® Surgical System. In: 2014 IEEE International Conference on Robotics and Automation (ICRA), 2014, pp. 6434–6439.
[9]Marcus, H. J., A. Hughes-Hallett, T. P. Cundy, G.-Z. Yang, A. Darzi, and D. Nandi. Da Vinci robot-assisted keyhole neurosurgery: a cadaver study on feasibility and safety. *Neurosurg. Rev.* 38(2):367–371, 2015.
[10]Marcus, H. J., K. Zareinia, L. S. Gan, F. W. Yang, S. Lama, G.-Z. Yang, and G. R. Sutherland. Forces exerted during microneurosurgery: a cadaver study. *Int. J. Med. Robot. Comput. Assist. Surg.* 10(2):251–256, 2014.
[11]McLeod, I. K., E. A. Mair, and P. C. Melder. Potential applications of the da Vinci minimally invasive surgical robotic system in otolaryngology. *Ear Nose Throat J.* 84(8):483–487, 2005.
[12]Meehan, J. J., and A. Sandler. Robotic repair of a Bochdalek congenital diaphragmatic hernia in a small neonate:

robotic advantages and limitations. *J. Pediatr. Surg.* 2007. https://doi.org/10.1016/j.jpedsurg.2007.06.013.

[13]Moorthy, K., Y. Munz, A. Dosis, J. Hernandez, S. Martin, F. Bello, T. Rockall, and A. Darzi. Dexterity enhancement with robotic surgery. *Surg. Endosc.* 18(5):790–795, 2004.

[14]Peirs, J., H. Van Brussel, D. Reynaerts, and G. De Gersem. A flexible distal tip with two degrees of freedom for enhanced dexterity in endoscopic robot surgery. In: The 13th Micromechanics Europe Workshop, 2002, pp. 271–274.

[15]Ryu, S. C., P. Renaud, R. J. Black, B. L. Daniel, and M. R. Cutkosky. Feasibility study of an optically actuated MR-compatible active needle. In: 2011 IEEE/RSJ International Conference on Intelligent Robots and Systems, 2011, pp. 2564–2569.

[16]Song, J., B. Gonenc, J. Guo, and I. Iordachita. Intraocular snake integrated with the steady-hand eye robot for assisted retinal microsurgery. In: 2017 IEEE International Conference on Robotics and Automation (ICRA), 2017, pp. 6724–6729.

[17]Swaney, P. J., P. A. York, H. B. Gilbert, J. Burgner-Kahrs, and R. J. Webster, III. Design, fabrication, and testing of a needle-sized wrist for surgical instruments. *J. Med. Device* 2017. https://doi.org/10.1115/1.403457.

[18]York, P. A., P. J. Swaney, H. B. Gilbert, and R. J. Webster. A wrist for needle-sized surgical robots. In: 2015 IEEE International Conference on Robotics and Automation (ICRA), 2015, pp. 1776–1781.